Applied Catalysis B: Environment and Energy 381 (2026) 125817

Contents lists available at ScienceDirect

Applied Catalysis B: Environment and Energy

journal homepage: www.elsevier.com/locate/apcatb

Carbon-induced metal growth and size-dependent activity in methane splitting on nickel nanoparticle catalysts for CO_x-free hydrogen production

Niloufar Atashi [a], Adrià Palomares [a], Nicola Verziaggi [b], Luis Alves [c,d], Adelio Mendes [c,d], Simone Meloni [b], Gonzalo Prieto [a,*]

[a] ITQ Instituto de Tecnología Química, Universitat Politècnica de València-Consejo Superior de Investigaciones Científicas (UPV-CSIC), Avenida de los Naranjos s/n, Valencia 46022, Spain
[b] Dipartimento di Scienze Chimiche, Farmaceutiche e Agrarie, Università Degli Studi di Ferrara, Via Luigi Borsari 46, Ferrara I-44121, Italy
[c] LEPABE - Laboratory for Process Engineering, Environmental, Biotechnology and Energy, Faculty of Engineering, University of Porto, Rua Dr. Roberto Frias, Porto 4200-465, Portugal
[d] ALiCE – Associated Laboratory in Chemical Engineering, Faculty of Engineering, University of Porto, Rua Dr. Roberto Frias, Porto 4200-465, Portugal

ARTICLE INFO

Keywords:
Methane decomposition
Turquoise hydrogen
Carbon-assisted particle growth
Operando XRD
Density functional theory

ABSTRACT

Catalytic methane splitting (CMS) to hydrogen and elemental carbon is a promising route to produce CO_x-free hydrogen, potentially achieving net carbon-negative output when using biogenic methane as the feedstock. On transition metal nanocrystals, especially Ni, CMS proceeds at lower temperatures (<1000 K) compared to (plasma-assisted) methane pyrolysis, additionally leading to higher added-value graphitic carbon nanostructure products. Earlier work has indicated that the size of the metal nanocrystals plays a central role for hydrogen (and carbon) production rates, however, conflicting results have been reported, possibly as a result of challenges associated to the deposition of the carbon products on the catalyst surface as well as phenomena like metal particle growth, fragmentation and deactivation. Herein metal nanocrystal size effects are assessed on the methane splitting reaction rate with a series of model supported Ni catalysts. A maximum methane splitting rate is attained for Ni nanoparticles with a diameter of ~10 nm at the onset of the reaction. *Operando* synchrotron X-ray diffraction and activity-specific transmission electron microscopy studies attribute the observed size effects on reaction rate to differences in the relative contribution of Ni nanocrystals larger and smaller than ca. 10 nm. This metal nanoparticle diameter represents a threshold minimum size for the effective nucleation and growth of graphitic carbon filaments, and therefore for sustained hydrogen production, which entails the lifting of Ni nanocrystals away from the oxide support in a carbon tip-growth mechanism. Moreover, *operando* studies reveal metal nanocrystal growth, which is specifically driven by the earliest methane splitting events on the catalyst surface, and determinant for the metal aggregation extent and intrinsic activity of the actual working catalyst. Density Functional Theory analyses identify *C and *CH_3 adspecies, emerging from CH_4 splitting on neat Ni surfaces, as central mediators to attain favourable energetics for the detachment of Ni adatoms from coordinatively unsaturated sites on the metal nanocrystals and their emission onto the oxide support material, hence responsible for a catalysis-driven Ostwald ripening metal growth mechanism. The results contribute to rationalize the interplay between metal nanocrystal size and carbon-metal dynamics to define an optimal Ni nanoparticle size of ~10 nm for a maximum hydrogen production rate, providing a blueprint for designing optimized catalysts for low-temperature methane splitting.

1. Introduction

Catalytic methane splitting (CMS), also referred to as methane cracking or decomposition, stands out as an example of utmost academic and technological interests[1,2]. This reaction plays a central role for the production of so-called *turquoise* hydrogen, derived from natural and shale gas. The process transforms carbon in the methane reactant to solid nanostructures, contributing to carbon fixation[3]. Remarkably, the overall process may become net carbon negative when applied to produce hydrogen from methane feeds of biogenic origin (biomethane)

* Corresponding author.
E-mail address: prieto@itq.upv.es (G. Prieto).

https://doi.org/10.1016/j.apcatb.2025.125817
Received 22 May 2025; Received in revised form 30 July 2025; Accepted 11 August 2025
Available online 12 August 2025
0926-3373/© 2025 The Authors. Published by Elsevier B.V. This is an open access article under the CC BY-NC-ND license (http://creativecommons.org/licenses/by-nc-nd/4.0/).

[4].

Catalytic methane splitting provides a lower-temperature, hence energetically less intensive, route to decomposing the recalcitrant CH_4 molecule (C-H bond energy >400 kJ mol^{-1}) in its elements, compared to non-catalytic or thermal plasma-assisted methane pyrolysis processes, which typically require operation temperatures in excess of 1200 K [5–7]. Furthermore, the use of supported nanocrystals, usually of 3d transition metals, as catalysts promotes the formation of tubular, graphitic carbon nanostructures as products. These structures feature significantly higher added value as components for electrically conducting and mechanically reinforced functional materials and composites, in contrast to less graphitic or amorphous carbon blacks or flakes which are commonly obtained under (plasma-assisted) methane pyrolysis conditions[7,8]. Therefore the former hold the potential to have an eminently positive impact on the technoeconomics of hydrogen production, particularly when cyclic interfacial hydrogenation enables semi-continuous process operation with periodic detachment and recovery of carbon filaments from the catalyst surface[9].

Metal nanoparticle size has been recognized as a central structural parameter in methane splitting catalysts. Previous studies have explored how the composition and texture of various oxide supports affect Ni dispersion and methane splitting activity. While some of these works asserted a significant impact of the support on performance[10–13], others have argued that methane splitting rates are primarily determined by the size of the Ni nanoparticles rather than the nature of the oxide carrier[14]. Both the initial reaction rate and deactivation rate have been analyzed in relation to the average metal nanoparticle or nanocrystal domain size. Consistently higher hydrogen production rates and extended catalyst lifetimes have been associated with relatively larger Ni nanocrystals in the sub-50 nm size regime[15–18]. However, occurrences such as metal particle sintering and crystallite fragmentation have also been inferred to occur for some catalysts under methane splitting conditions, which may potentially obscure size-dependent phenomena[18–20].

Unveiling nanoparticle size effects is crucial for advancing the rational design and optimization of methane-splitting catalysts. However, their study poses a heightened challenge for CMS compared to standard structure sensitivity studies of catalytic reactions on solid surfaces. On the one hand, the fast accumulation of solid carbon products on the catalytically active metal surfaces in this gas-to-solid reaction introduces additional solid-solid interactions between the catalyst and the product, which may also exhibit size dependence. On the other hand, transport phenomena have been proposed to be kinetically relevant, either on the surface, across graphite-metal interfaces[21], or even in the bulk, across the lattice of the active metal[22]. These considerations make it difficult to analyze methane splitting under the prism of established structure sensitivity phenomena, which often emerge as a result of the predominant involvement of specific surface facets or motifs in at least one kinetically relevant surface reaction step[23–27].

Herein we investigate the effect of nanocrystal size on the intrinsic methane splitting reactivity on model supported Ni catalysts. Pre- and post-reaction activity-specific metal nanoparticle size analyses are combined with complementary *operando* synchrotron X-ray diffraction studies and first-principles Density Functional Theory calculations. The results elucidate plausible molecular mechanisms underlying a catalysis-driven metal sintering, which is strongly associated with the unconventional nanocrystal size effects exhibited by the reaction, which maximizes mass-specific hydrogen production rate for a Ni nanoparticle size of ca. 10 nm.

2. Experimental

2.1. Synthesis of supported Ni catalysts

High-purity SiO_2 gel materials with spherical primary particle morphology (d_{pore}=6–30 nm, Silicycle), high-purity γ-Al_2O_3 materials (d_{pore}= 4–150 nm), synthesized by dehydration of pseudo-boehmite Pural SB1, 200 and Disperal 80 precursors (Sasol Materials) at 823 K for 5 h under a stagnant air atmosphere, and bare (non-porous) nanospherical Al_2O_3 ($d_{particle}$=50 nm, Nanophase, hereafter denoted *np*-Al_2O_3) were applied as catalyst supports as received, without further modifications. Nickel was incorporated on the SiO_2 and Al_2O_3 carrier materials by impregnation with a 4.0 M aqueous solution of Ni$(NO_3)_2$·6 H_2O (Merck, 99.999 %) in 0.1 M HNO_3. Experimentally, the support material (in powder form) was dried at 423 K under dynamic vacuum (10 mbar) for 3 h in a multi-neck round-bottom flask. Next, the Ni nitrate solution was infiltrated into the porosity of the support under static (residual) vacuum. The volume of impregnating solution applied was equivalent to 90 % of the total mesopore volume of the support material as determined by N_2 physisorption. The impregnate was dried under dynamic vacuum (10 mbar) overnight, and the dried solid was loaded into a packed-bed quartz tubular reactor, inserted axially into a vertical tubular oven. Next, the metal precursor was transformed into nickel oxide crystallites via a NO-assisted nitrate decomposition route developed earlier by de Jong and coworkers[28], heating to 623 K for 3 h under top-down flow of 2 % NO/He (vol%, Linde), using a heating rate of 2 K·min^{-1} from room temperature. Model catalysts consisting of Ni nanocrystals deposited on the outer surface of *np*-Al_2O_3 nanobeads were synthesized following a similar procedure. In this case, due to the lack of intraparticle (meso)porosity in the carrier materials, Ni was applied by wet impregnation. The amount of Ni$(NO_3)_2$·6 H_2O to attain a preset Ni loading on *np*-Al_2O_3 in the range of 1–30 wt%, was dissolved in 50 mL Milli-Q water. The corresponding mass of the support material was slurried into the metal precursor solution and the suspension stirred for 1 h at RT. Next, the water solvent was removed by evaporation in a rotary evaporator operating at 5 mbar and 333 K. The solid recovered was dried overnight at 373 K in a convective oven and the metal nitrate precursor decomposed under the flow of 2 %NO/He as detailed above. Catalysts have been denoted as Ni/SM (*x* nm), where SM denotes the oxide support material and *x* the average Ni nanoparticle size as determined by scanning transmission electron microscopy following reduction activation.

2.2. Catalytic methane splitting

Catalytic methane splitting tests have been carried out in an automated catalyst testing setup (PIDEng, Micromeritics). The setup features high-precision mass flow controllers (F-211CV-100-MAD-11K, Bronkhorst) for gas feeding. Catalysts were loaded in microparticulate form on a quartz frit inside a quartz reactor with an inner diameter of 10 mm. Then, the reactor was inserted axially into a vertically oriented annular convection oven connected to a PID temperature controller. The oven as well as all gas transfer lines up- and down-stream of the tubular reactor are hosted in a heated box featuring a fan for air recirculation and maintained at 423 K. The gas outlet stream leaving the reactor was sampled by a mass spectrometer (Omnistar, Pfiffer) equipped with a transfer line heated to 473 K and Faraday and SEM detectors. The catalyst was initially activated *in situ* by a metal reduction treatment under the flow of 20 % H_2/He (99.9999, Linde) at 873 K for 5 h (heating ramp from RT of 2 K·min^{-1}) at atmospheric pressure. This reduction temperature was selected based on H_2-temperature programmed reduction profiles and it rendered the metal into the catalytically active metallic state. After metal reduction was complete, the reactor was flushed and filled with He and isolated offline by means of a multiport valve which directs the incoming gas flow to a bypass line. Next, a gas feed flow of 95 %CH_4/Ar (Linde, certified mixture, 100 mL·min^{-1}) diluted in He (Linde, > 99.99 %, 50 mL·min^{-1}) was stablished through the bypass line and the He-filled reactor heated to the preset reaction temperature (873 K) using a heating rate of 2 K·min^{-1}. Then, the reaction was initiated by a valve switch which directs the methane feed stream to the reactor's inlet. During the test, outflow gases were analyzed by the online mass spectrometer previously calibrated by

injecting selected mixtures of 5 % Ar/CH_4 and H_2. To limit cumulative carbon deposition on the catalyst bed and prevent clogging of gas flow paths and pressure build-up in the reactor, as well as to restrict the growth of carbon filaments and ensure reliable statistical analysis of post-catalysis catalyst evaluations via TEM, the total time-on-stream was limited to 5 min. Note that longer testing times resulted in reactor clogging and, in some cases, quartz burst events and this should be carefully observed for safe operation. Moreover, in order to investigate intrinsic activity, without contributions from catalyst deactivation, initial (extrapolated to zero time on-stream) hydrogen production rates were determined from the composition of the outlet gas stream using Ar as an internal standard based on methane consumption rates using Eq. 1.

$$\boldsymbol{r}_{H_2} = \mathbf{2}\cdot\left(-\boldsymbol{r}_{CH_4}\right) = \mathbf{2}\cdot\frac{\boldsymbol{X}_{CH_4}\cdot\boldsymbol{W}_{CH_4}}{\boldsymbol{M}_{cat}} \quad (1)$$

Where $\boldsymbol{r}_{H_2}$ is the rate of H_2 formation, $-\boldsymbol{r}_{CH_4}$ is the rate CH_4 conversion, $\boldsymbol{X}_{CH_4}$ stands for the methane conversion per reactor pass, $\boldsymbol{W}_{CH_4}$ is the molar flow of methane, and $\boldsymbol{M}_{cat}$ is the mass of catalyst .

2.3. Characterization methods

Textural properties of oxide support materials were assessed by nitrogen physisorption. Physisorption isotherms were recorded using a Micromeritics ASAP instrument after degassing the solid sample (ca. 100 mg, sieve fraction 0.6–0.8 mm) at 523 K under vacuum for 10 h. Specific surface areas were derived using the B.E.T method in the relative pressure (P/P_0) regime of 0.05–0.30. Total mesopore volumes were based on the N_2 uptake at a relative pressure P/P_0 of 0.95.

Ex situ powder X-ray diffraction (XRD) was applied to assess the presence and nature of crystalline phases as well as to quantify the average metal (oxide) crystalline domain size in catalysts at various stages of their synthesis and activation procedures. XRD patterns were recorded in Bragg-Brentano geometry using a PANalytical CUBIX diffractometer using Cu Kα radiation ($\lambda_1 = 1.5406$ Å, $\lambda_2 = 1.5444$ Å, $I_2/I_1 = 0.5$) operating at 45 mA and 40 kV. The length of the goniometer arm was 200 mm and a fixed divergence slit with an aperture of 1/8° was used. The measurement was performed at 298 K, with the sample rotating at 0.5 revolutions per second during the measurement. The scanning range was from $2\theta = 3.5^{\circ}$ to 90.0°, with a step of 0.020° and an acquisition time of 35 s per step. To determine the crystallite size, the Scherrer equation with a crystal shape factor of $k = 0.9$ was applied to the Ni (111) diffraction line for metallic nickel and the NiO (200) diffraction line for nickel oxide, respectively, unless stated otherwise. Oxidic (as-synthesized) catalysts were mounted on stainless-steel round holder. Following *ex situ* reduction activation in flow of H_2 at 873 K, catalysts were passivated by 1 % O_2/He and then mounted onto a stainless-steel round sample holder.

The evolution of Ni crystallite size was also assessed *operando*, under relevant methane splitting reaction conditions, using synchrotron radiation-XRD (SR-XRD). Catalytic methane splitting tests were conducted in a spectroscopic capillary flow cell reactor at the NOTOS (BL16) beamline station of the ALBA synchrotron light source (Spain). The setup comprises a 10 cm length quartz glass capillary with 10 μm wall thickness and 0.98 mm Ø ID. It features a total void volume of ca. 17 mL and a high-precision gas feeding system based on mass-flow controllers (F-201CM-PAD-88-K, Bronkhorst). A sieve fraction of the catalyst sample (100 −200 μm) was loaded at the center of the quartz glass capillary and packed between two packed-beds of silicon carbide granules (100 −200 μm) to ensure the development of a consistent gas-solid flow dynamics as well as the preheating of the incoming gas stream upstream of the catalyst packed-bed. Two quartz wool plugs, placed on both sides of the SiC granule beds, prevented the solids from being dragged downstream by the gas flow. The capillary was mounted horizontally onto a flow cell and aligned with the X-ray beam (100 μm x 100 μm). The catalyst bed was heated by a hot air blower (Mistral System 230 V/3400 W, nozzle Ø 50 mm ID, Leister®) positioned orthogonal to the capillary, providing an isothermal packed bed length of 5 mm. X-ray diffraction patterns were collected using an incident photon energy of 13 keV ($\lambda = 0.9537$ Å) with a time resolution of 2 min·scan^{-1}. Measurements were performed in a Debye-Scherrer geometry using a Mythen-II position-sensitive detector (6 modules at 535 mm from the sample) in the 2θ range of 10–50 degrees, corresponding to a Q range of 1.2–5.6 Å^{-1}. Before the *operando* methane splitting test, catalyst reductive activation was performed *in situ*, and monitored with XRD to track the reduction of the Ni species and to assess the Ni^0 crystallite size distribution in the as-activated catalyst. The sample was reduced at 873 K for 90 min with a heating ramp of 2 K·min^{-1} under a 20 %H_2/He gas stream (1.2 mL·min^{-1} H_2 and 4.8 mL·min^{-1} He, Linde, >99.99 %). Next, the cell was flushed with He (Linde, >99.99 %, 6 mL·min^{-1}) for 15 min to purge hydrogen from the system. Catalytic methane splitting was performed at 873 K by accepting into the cell a flow of 67 % CH_4/He (3.4 mL·min^{-1} CH_4 and 1.85 mL·min^{-1} He, Linde, >99.99 %), corresponding to a gas space velocity of 0.45 mol CH_4·mol$_{Ni}^{-1}$·min^{-1}. The reaction was performed for 30 min under isothermal conditions, while registering the XRD patterns and online monitoring the downstream gas composition using a CIRRUS-3-XD mass spectrometer (MKS) connected to the outlet of the capillary. Finally, the cell was flushed again with He (Linde, >99.99 %, 6 mL·min^{-1}) for 15 min and the catalyst packed bed let cool down to RT. X-ray diffraction patterns were continuously collected in the Q range of 1.2–5.6 Å^{-1} as detailed above. Line broadening and shape analysis has been applied to determine metal crystallite size distributions using a double-Voigt integral-breadth analysis[29] on Ni(111) and Ni(200) diffractions.

The nanoscale structure of catalysts, as well as solid carbon products following methane splitting experiments, was studied with (Scanning-) Transmission Electron Microscopy (S)TEM. Ni catalysts were first activated *ex situ* by H_2 reduction at 873 K (5 h) and the resulting Ni nanocrystals were surface passivated by exposure to flow of 1 %O_2/He at RT for 1 h. Next, catalysts were embedded in a low-viscosity epoxy resin (Spurr, Merck) and the latter cured at 343 K overnight. Then sections with a nominal thickness of ca. 150 nm were produced from the embedded specimens using a Diatome 35° knife mounted on a Reichert-Jung Ultracut microtome, and the sections collected on Cu TEM grids coated with a Formvar film and a carbon overlay. In the case of Ni/*np*-Al_2O_3 powder samples were directly dry-cast onto the TEM grids. Following exposure to methane splitting reaction conditions, the catalysts were recovered from the fixed bed reactor (after flushing with He for 30 min) and kept in a glove box under the exclusion of air (<1 ppm O_2, <1 ppm H_2O). Microscopy experiments were performed in a JEOL JEM2100F microscope operating at 200 kV.

Additional details on physicochemical characterization methods and the determination of initial CMS hydrogen production rates are provided in the Supporting Information.

2.4. Computational methods

Periodic DFT simulations were performed using the Vienna Ab initio Simulation Package (VASP 6.4.0) [30,31] within the Perdew-Burke-Ernzerhof (PBE)[32] approximation of the density functional theory coupled with the projector-augmented wave (PAW) method [33]. Kohn-Sham orbitals have been expanded on a plane wave basis set with a kinetic energy cutoff of 400 eV and a convergence criterion for the self-consistent field calculations (SCF) $1.0\cdot10^{-6}$ eV on the energy variation between successive steps. The surface of *fcc* Ni nanocrystals was modelled by a 3 × 3 Ni(111) slab consisting of 4 at. layers, whereas the Al_2O_3 oxide carrier was modelled by a 2 × 2 γ-Al_2O_3(100) slab consisting of 4 (stoichiometric) layers. The slabs were spaced by a 12 Å vacuum layer along the z axis to avoid spurious interactions between periodic replicas. In geometry optimization atomic positions are relaxed according to the conjugate gradient method. The top two atom layers and all adsorbates were allowed to relax, whereas the bottom two

slab atom layers were fixed to emulate bulk effects. The Brillouin zone was sampled by a 4x4x1 Monkhorst-Pack k-point grid[34] for stepped Ni (111) slab and step structures, and a 3x3x1 grid for kinked Ni surfaces and γ-Al_2O_3.

3. Results and discussion

3.1. Manipulation of Ni nanocrystal size

As a result of differences in the available mesopore volume of the SiO_2 carrier materials, which determined the metal precursor uptake at the impregnation step of catalyst synthesis, the experimental nickel loading in the set of Ni/SiO_2 materials was in the range of 12–21 wt% (Table S1 in the Supporting Information). As determined by X-ray diffraction, the average NiO crystallite size evolved systematically in the range of 4–23 nm for this series of supported catalysts (Figure S1 in the Supporting Information). H_2-temperature programmed reduction was applied to probe the reduction behavior of the supported NiO crystallites. Metal oxide reduction events downshifted systematically from ca. 670 K to 590 K on increasing the average NiO crystallite size from 4 to 23 nm (Figure S2), indicating that smaller oxide nanocrystals are harder to reduce, likely owing to a higher chemical interaction with the SiO_2 support material. Based on the H_2 reduction profiles, which showed H_2 consumption to cease above 800 K, a temperature of 873 K was selected for reductive activation prior to catalysis, i.e. to render Ni into its zerovalent state. Following H_2 reductive activation to metallic nickel species, the systematic evolution of crystallite size across the series of catalyst materials was preserved, with $d(Ni^0)$ spanning in the range of 2–31 nm (Figure S3).

Ni nanoparticle size was assessed using high-angle dark-field scanning-transmission electron microscopy (HAADF-STEM) on nm-thick cross-sections of the activated catalysts. Fig. 1 shows representative HAADF-STEM micrographs and the corresponding Ni nanoparticle size histograms. Microscopy observation confirmed the systematic variation of Ni^0 nanoparticle size across the series of catalysts, with monomodal size distributions in all cases. Comparatively narrower size distributions were determined for the smallest nanocrystal sizes, which broadened progressively as the average Ni nanoparticle size increased. Similarly, metal nanoparticle size was systematically adjusted for an additional series of Ni/Al_2O_3 catalysts supported on mesoporous γ-Al_2O_3 (Figure S5). The methodical variation of Ni nanocrystal size rendered this set of catalysts ideal to assess metal size effects in methane splitting catalysis.

3.2. Catalytic methane splitting

The activity of the series of supported Ni catalysts for catalytic methane splitting was assessed under relevant operation conditions at 873 K. To minimize contributions from carbon deposition and catalyst deactivation, hence to probe the intrinsic catalytic performance, the assessment was restricted to the initial activity, i.e. extrapolated to zero

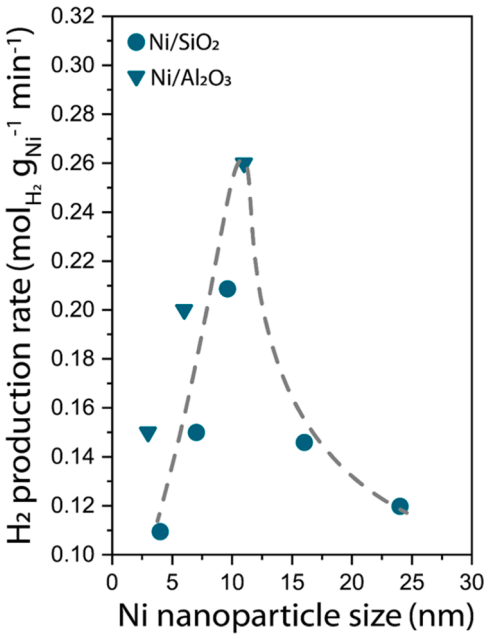

Fig. 2. Evolution of the metal-specific hydrogen production rate, with the average Ni^0 nanoparticle diameter in the activated catalyst, i.e. following reduction, for a series of Ni/SiO_2 and Ni/Al_2O_3 supported catalysts with monomodal Ni particle size distributions. Reaction conditions: tubular quartz reactor, $T = 873$ K, $P = 0.1$ MPa, feed composition Ar:CH_4:He 1:19:10 vol. The dashed line is added as a guide to the eye.

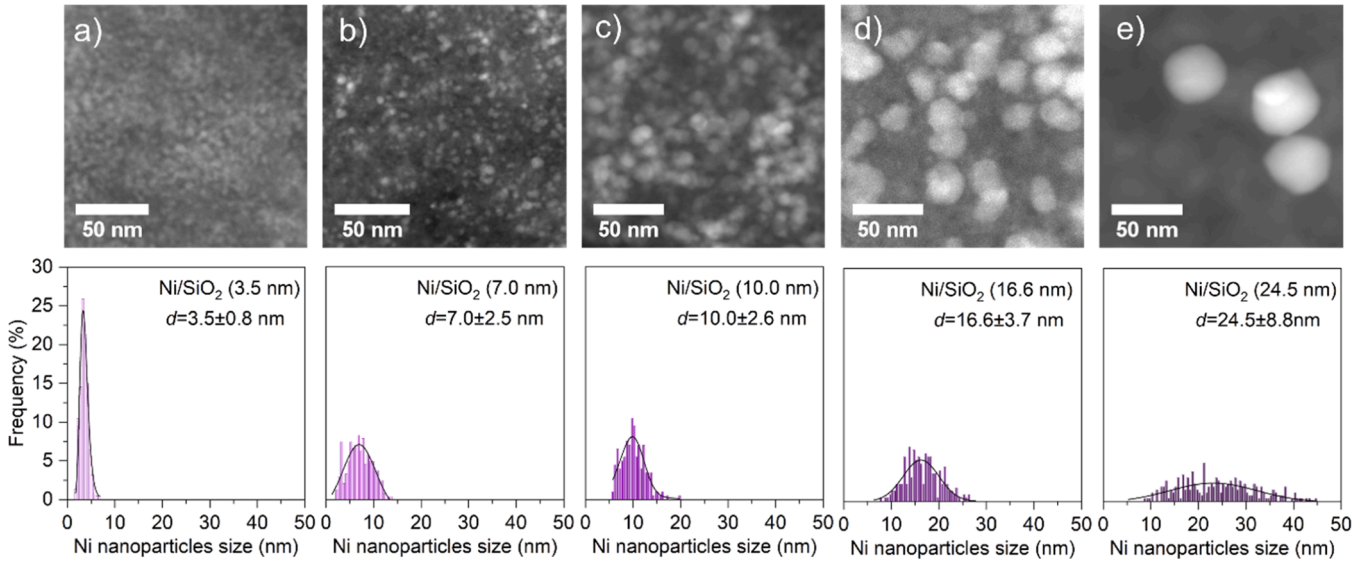

Fig. 1. Representative cross-sectional HAADF-STEM micrographs (top) and the corresponding Ni^0 nanoparticle size histograms (bottom) for the series of Ni/SiO_2 catalysts, with varying Ni^0 nanoparticle size, following reductive activation in flow of 20 %H_2/He at 873 K. **a)** Ni/SiO_2 (3.5 nm); **b)** Ni/SiO_2 (7.0 nm); **c)** Ni/SiO_2 (10.0 nm); **d)** Ni/SiO_2 (16.6 nm); **e)** Ni/SiO_2 (24.5 nm). Additional micrographs are provided in Fig. S4 in the Supporting Information.

time-on-stream. Fig. 2 shows the evolution of the mass-specific hydrogen production rate as a function of the Ni nanocrystal size. As observed, a volcano dependence was observed for the reaction rate with the average metal nanoparticle size, reaching an apex maximum rate for a Ni nanoparticle size of ca. 10 nm. For the reasons outlined above in the introduction, i.e. the expected kinetic significance of surface/bulk transport phenomena or the (permanent) coverage of metal sites by the solid carbon reaction product, the classical *turnover frequency* (TOF) concept may likely not be fully transferable to methane splitting. Deriving an *apparent* TOF based on the experimental initial methane splitting rates and the amount of Ni surface sites exposed on the surface of the catalyst as determined by hydrogen chemisorption following reduction activation, i.e. prior to reaction, renders a linear upward trend (Figure S6), which is in line with correlations derived earlier from a survey of literature data[35]. Remarkably, both SiO_2- and Al_2O_3--supported catalysts fall essentially on the same trend, supporting the fact that methane splitting activity correlates with the metal nanoparticle size and it is less, if at all, dependent on the specific nature of the oxide support material. This Ni nanoparticle size effect on reaction rate is unconventional, and it defies explanation based on classical structure sensitivity phenomena, in line with the proposal above that the TOF concept may not be transferable to methane splitting[36]. Indeed, a linearly scaling (apparent) TOF cannot account for the experimentally observed volcano-type trend in mass-specific activity as a function of nanoparticle size. As discussed further in this article, this apparent discrepancy arises because not all of the metal surface area measured by chemisorption prior to catalysis contributes to the observed hydrogen production rate. This is due to early-stage metal sintering and the encapsulation of metal nanoparticles by carbon deposits during the initial stages of the catalytic reaction (*vide infra*).

3.3. Size-dependent carbon filament development

To gain deeper insight into the unconventional size effects on reactivity, ensuring unobstructed access to the interface between the Ni nanocrystals and the carbon deposits through electron microscopy techniques was deemed crucial. This remains a challenge with conventional catalysts, such as in the above series of Ni/SiO_2 and Ni/Al_2O_3 catalysts, where the metal nanocrystals are confined within the mesopores of the support material. To address this challenge, a third set of model catalysts was employed, synthesized by depositing Ni nanocrystals on the outer surface of non-porous Al_2O_3 nanobeads (*np*-Al_2O_3). The support material offers a nanostructure based on bare spherical nanoparticles with sizes spanning in the range of 10–80 nm, while XRD analysis showed the prevalence of δ-Al_2O_3 (*P-1*) and γ-Al_2O_3 (*Fd-3m*) transitional alumina polymorphs (Figure S7). In the absence of templating effects by mesopores, control over the Ni nanocrystal size for this series relied on adjustment of the Ni loading on the alumina carrier (Figure S8). As shown in Fig. 3, following reductive activation, Ni nanoparticles appeared supported on the outer surface of the Al_2O_3 nanobeads, hence readily accessible to microscopy inspection. Satisfactorily, the series of Ni/*np*-Al_2O_3 model catalysts also presented monomodal metal particle size distributions and a systematic variation in average Ni nanoparticle size over the range of 3–20 nm.

The nanostructure of the Ni/*np*-Al_2O_3 model catalysts was also assessed following their exposure to methane splitting reaction conditions. Bright-field high-resolution TEM was applied in this case. This enables imaging not only the supported Ni nanocrystals but additionally carbon species, which accumulate on the catalyst surface as a result of the methane splitting reaction, and which display too low *Z*-contrast in HAADF-STEM. Fig. 4**a-d** shows representative TEM micrographs for this set of catalyst following exposure to methane splitting conditions.

The corresponding Ni nanoparticle size histograms recorded after catalysis were compared to those of the catalysts in their as-activated state, i.e., after H_2 reduction, for catalysts with varying initial Ni nanoparticle sizes. (Fig. 4**e-h**). The growth of Ni nanoparticles was evident, as indicated by the broadening of the size histograms, which extend beyond 20 nm in all cases after exposure to CMS conditions. Moreover, the analysis disclosed the existence of two distinct populations of Ni nanoparticles subsequent to exposure to reaction conditions. Firstly, Ni nanoparticles were identified at the tip of carbon filaments, indicating detachment from the Al_2O_3 support, i.e. a characteristic feature associated with the tip-growth mechanism that typically dominates under methane splitting reaction conditions[37]. These nanoparticles are consequently linked to a sustained production of carbon (and hydrogen) and are henceforth denoted as *productive* nanocrystals. A similar carbon growth mode was observed with Ni catalysts supported on mesoporous carrier materials, i.e. Ni/SiO_2 and Ni/Al_2O_3. However, for the series of Ni/*np*-Al_2O_3 model catalysts, the absence of pore confinement enabled the imaging also of a second set of metal nanoparticles which, on the contrary, remained on the surface of the Al_2O_3 support and exhibited no association with filamentous carbon

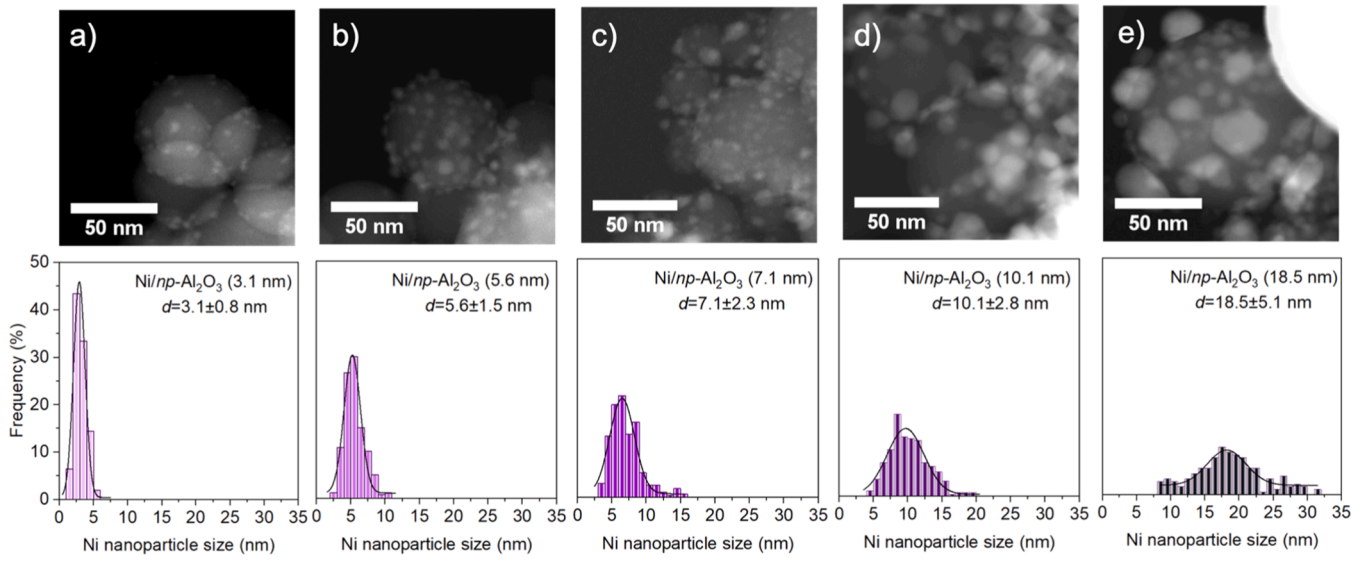

Fig. 3. Representative HAADF-STEM micrographs (top) and the corresponding Ni nanoparticle size histograms (bottom) for the series of Ni/*np*-Al_2O_3 model catalysts, with varying Ni^0 nanoparticle size, following reductive activation in flow of 20 %H_2/He at 873 K. **a)** Ni/*np*-Al_2O_3 (3.1 nm); **b)** Ni/*np*-Al_2O_3 (5.6 nm); **c)** Ni/*np*-Al_2O_3 (7.1 nm); **d)** Ni/*np*-Al_2O_3 (10.1 nm); **e)** Ni/*np*-Al_2O_3 (18.5 nm). Additional micrographs are provided in Fig. S9 in the Supporting Information.

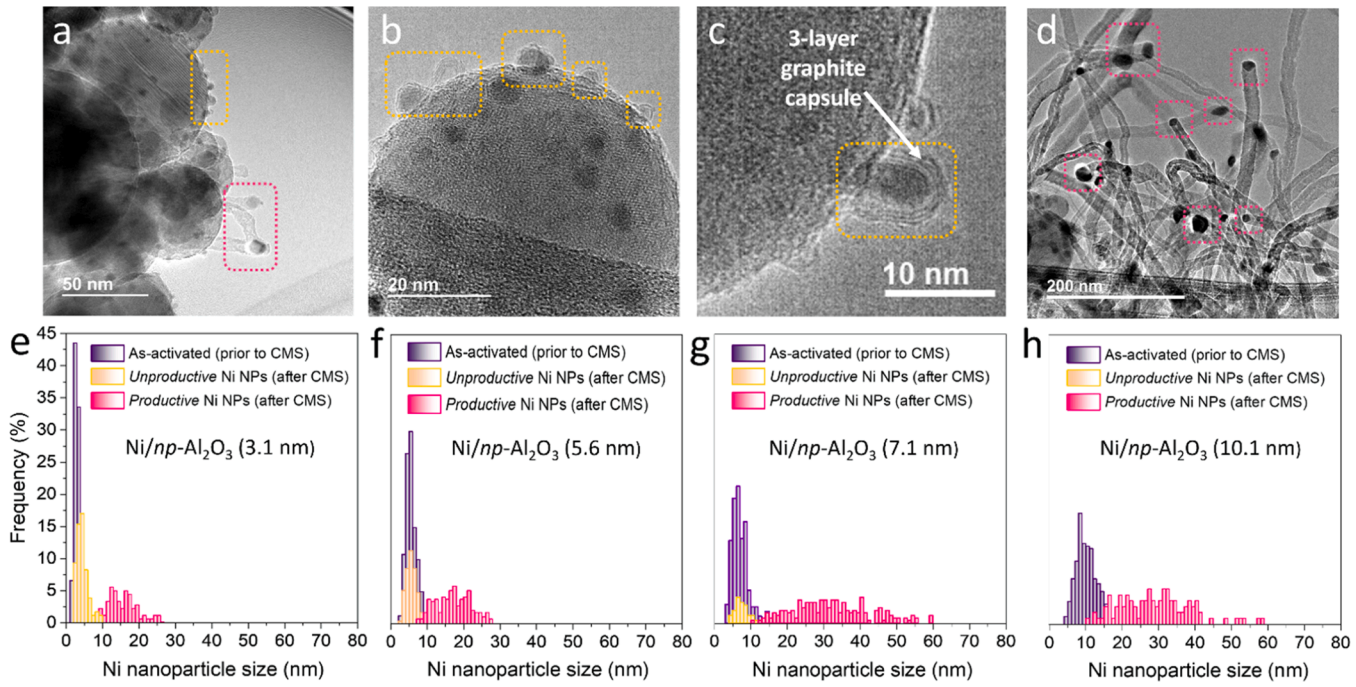

Fig. 4. a-d) Representative bright-field TEM micrographs for Ni/*np*-Al_2O_3 (3.1 nm) model catalyst following exposure to catalytic methane splitting reaction conditions for 5 min, time-on-stream. The dashed pink areas mark *productive* Ni nanoparticles (>8 nm) at the tip of carbon filaments, while yellow dashed marks show the presence of smaller (<10 nm) *unproductive* nanoparticles, which become swiftly inactivated by few carbon layers in the course of the first reaction turnovers and thus do not sustainably contribute to the overall hydrogen production rate. **e-h)** Population-specific Ni nanoparticle size histograms for Ni/*np*-Al_2O_3 catalysts, showing *productive* Ni particles (pink) and *unproductive* Ni nanoparticles (yellow). For reference, the corresponding particle size histograms for the catalysts in their activated state, i.e. following reduction and prior to exposure to CMS reaction conditions, are also included (purple color). The corresponding histogram for Ni/*np*-Al_2O_3 (18.5 nm) is provided in Fig. S10, in the Supporting Information.

structures. This second population of Ni nanocrystals is presumed to have made minimal contributions to the macroscopically observed methane splitting rate, and therefore, they are designated as *unproductive*. Detailed examination of the outer surface of the latter Ni nanocrystals uncovered the existence of a limited number (1–3 layers) of graphitic carbon enveloping the metal (Fig. 4**c**). From this observation, it is conjectured that the inefficiency of these Ni nanocrystals in driving the reaction is not inherently linked to an inactivity towards methane splitting. Instead, this is attributed to their inability to initiate filamentous carbon structures, leading to premature deactivation caused by encapsulation in carbon deposits from the initial reaction turnovers on the metal nanocrystal surface.

Furthermore, microscopic inspection unequivocally revealed marked and systematic size differences between *productive* and *unproductive* Ni nanocrystals. This is prominently illustrated in the population-specific size histograms provided in Fig. 4**e-h**, where the normalized contributions from each set of Ni nanoparticles are distinctly portrayed. *Productive* Ni nanoparticles consistently exhibited sizes surpassing approximately 8–10 nm, irrespective of the initial average Ni nanoparticle size determined for the catalyst in its as-activated state, i.e. before catalysis. For catalysts with initial average Ni particle sizes < 7 nm, *productive* particles showed sizes predominantly in the range from 10 to 30 nm after exposure to methane splitting conditions, while their size extended up to > 50 nm in the case of catalysts featuring initial average Ni nanoparticle sizes ≥ 7 nm. Besides, the nanostructure of the carbon product showed a dependence on the average size of the *productive* Ni nanoparticles located at the tip of the carbon filaments, with Ni particles averaging sizes ≥ 20 nm leading to CNF with greater graphitization degree and fewer structural defects, as probed with Raman spectroscopy (Figure S11). In stark contrast, *unproductive* Ni nanocrystals consistently showed sizes < 10 nm in all cases. These findings strongly support the notion that a minimum nanocrystal size of approximately 10 nm is indispensable for carbon filament growth, thereby sustaining reaction activity and preventing premature metal encapsulation.

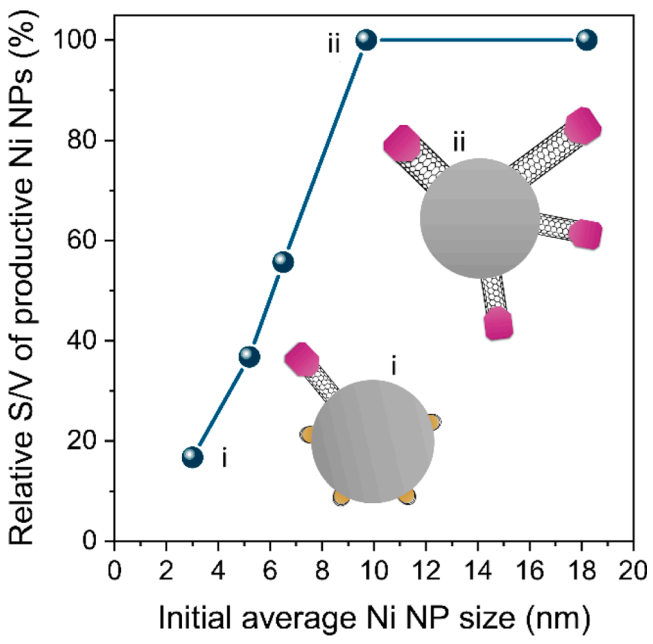

Fig. 5. Evolution of the volume-specific surface contribution from *productive* Ni nanoparticles, i.e. associated to carbon filament growth, as derived from the population-specific Ni particle size histograms, with the initial average Ni nanoparticle size before exposure to the methane feed. Reaction conditions: tubular quartz reactor, $T = 873$ K, $P = 0.1$ MPa, feed composition Ar:CH_4:He 1:19:10 vol. The insets in the figure illustrate the relative abundance of different types of Ni nanoparticles at selected points throughout the evolution.

As shown in Fig. 5, the relative specific surface contribution from the productive Ni nanocrystal populations, derived from geometric analysis of the population-specific metal nanoparticle size histograms, correlated with the average Ni nanoparticle size in the as-activated catalyst, prior to exposure to reaction conditions. The contribution from productive nanoparticles surged from a modest 17 % in the case of Ni/*np*-Al_2O_3 (3.1 nm) to become 100 % for catalysts featuring initial average Ni nanoparticle sizes $\geq$ 10.1 nm. For larger initial Ni average particle sizes, carbon-encapsulated Ni nanocrystals were no longer observed on the surface of the *np*-Al_2O_3 carrier.

Based on the relative specific surface contributions of the two Ni nanoparticle populations, and assuming a surface atom density of 38.2 atoms·nm^{-2} for the few-layer graphene (approximated as three layers) encapsulating the unproductive nanoparticles, along with a carbon filament mass density of 2.1 g·cm^{-3} for those grown from the productive metal nanocrystals, the mass contribution of the former type of carbon was found to be negligible (<1 %), already after the limited filament growth achievable during the relatively short 5-minute methane splitting reaction time.

These observations indicate that the macroscopically observed size effects on reaction rate can be ascribed to differences in the relative contribution from Ni nanocrystals exhibiting sizes above and below the threshold size of ca. 10 nm on the working catalyst. On the one hand, catalysts with a larger fraction of smaller, *unproductive* Ni nanocrystals exhibit lower overall methane splitting rate owing to a significant fraction of the metal surface area being not effectively contributing a sustained hydrogen production. On the other hand, for catalysts showing initially Ni nanoparticles with diameters equal or higher than 10 nm, essentially all metal nanoparticles lead to the growth of a carbon filament, thereby contributing to the overall hydrogen production rate. In this case, nanoparticle diameter progressively larger than 10 nm result in progressively lower specific metal surface area, which results also in a decline in hydrogen production rate. Striking a balance between the fractional contribution from productive Ni nanoparticles and mass-specific Ni surface area, an average Ni nanoparticle size of ca. 10 nm resulted in maximal metal-specific hydrogen production rates, irrespective of the nature of the oxide support material.

Previous studies, based on computational analyses, have proposed that a minimum metal cluster size is necessary to achieve favorable energetics for the detachment of graphitic overlays, a crucial step for carbon filament growth[38,39]. These studies primarily focused on a base-growth mechanism where carbon nanotubes grow away from static metal nanoparticles. Our results indicate that size constraints also apply to tip-growth mechanisms, which are commonly observed in CH_4 splitting catalysis.

3.4. Methane splitting-driven metal nanocrystal growth

A fundamental observation, seemingly pivotal for sustaining methane splitting with initially highly dispersed Ni catalysts, is the growth of metal nanoparticles. Consequently, additional insights into this phenomenon have been gleaned through a combination of complementary *operando* experimental and computational investigations.

Growth of Ni nanocrystals during the earlier stages of the methane splitting reaction was monitored using *operando* high-resolution X-ray diffraction with synchrotron radiation in a capillary cell equipped with a packed-bed microreactor (Figure S12). Catalyst Ni/*np*-Al_2O_3 (7.1 nm), featuring an initial Ni nanoparticle size of ca. 7 nm, was selected for this analysis to ensure a negligible contribution from excessively small, XRD-silent crystallites (d<3 nm). Fig. 6**a,b** show the temperature-resolved evolution of the XRD pattern during the *in situ* reductive catalyst activation under the flow of 20 %H_2/He. In a narrow 2θ range of 26–27.3°,

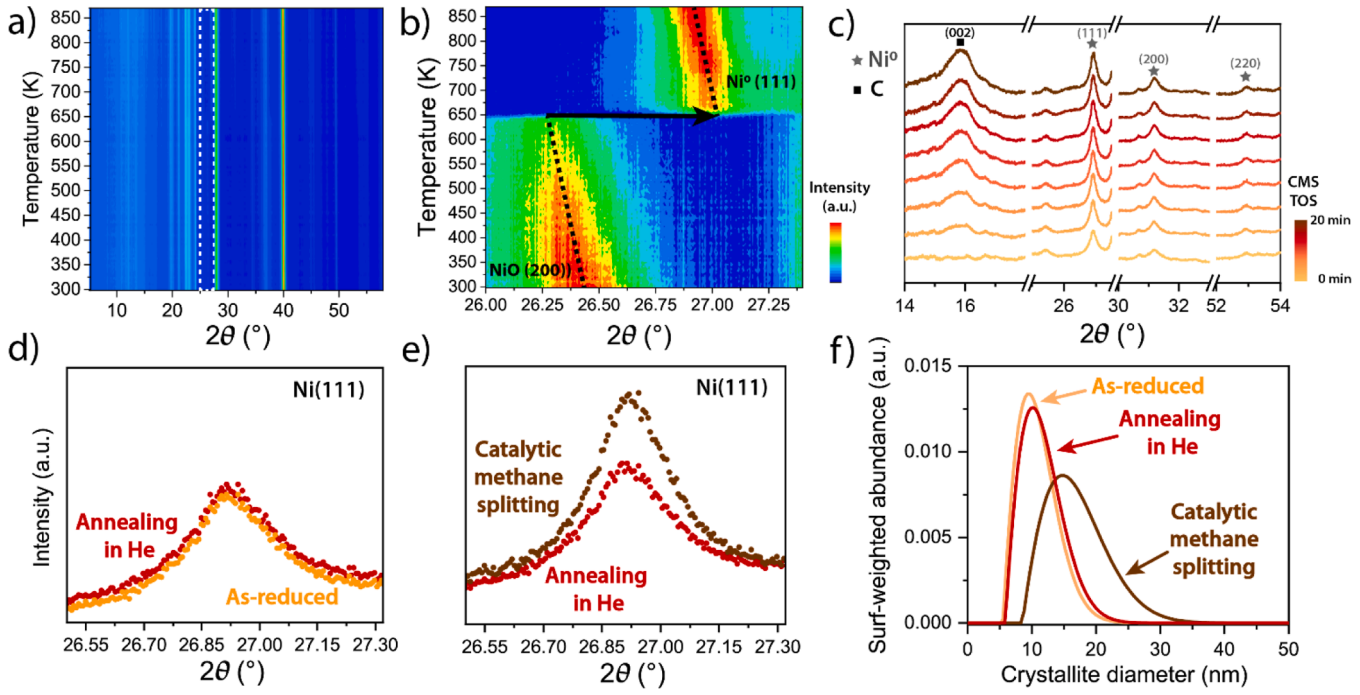

Fig. 6. a,b) Temperature-resolved synchrotron-radiation powder X-ray diffraction patterns recorded for Ni/*np*-Al_2O_3 (7.1 nm) in a capillary microreactor during *in situ* reduction activation by heating under H_2 flow from room temperature to 873 K, and **c)** *operando,* during catalytic methane splitting reaction. Reaction conditions: T = 873 K, P = 0.1 MPa, gas feed composition CH_4:He 2:1 vol, maximum time-on-stream (TOS) = 20 min. Panel b provides a blown-up view of the region marked with a dotted frame on panel a, showing the reduction of NiO to metallic Ni. In panel c, the x-axis has been broken to facilitate visualization of diffractions associated to Ni in the presence of intense diffractions from the Al_2O_3 support material. **d,e)** Close-up views showing changes at the Ni(111) diffraction line during **d)** annealing of the *in situ* activated catalyst in flow of inert He at 873 K or **e)** further exposing the catalyst to catalytic methane splitting conditions at 873 K. **f)** Evolution of the Ni^0 crystallite size distribution, as determined by a double-Voigt integral-breadth analysis[29] of line broadening and shape for Ni^0 diffractions, showing that Ni crystallite growth does not take place in inert He atmosphere, but upon exposure of the catalyst to the high carbon chemical potential pertaining to the catalytic methane decomposition reaction at 873 K.

NiO (00–044–1159) diffraction lines in the catalyst oxidic precursor vanished, while signals for *fcc* Ni^0 (00–004–0850) emerged, indicative of metal reduction. At the final temperature of 873 K, only diffractions for *fcc* Ni^0 were discernible, confirming the reductive activation of the catalyst.

Next, the *in situ* activated catalyst was flushed with He at 873 K for 10 min. Following this, a reactant gas mixture of 67 % CH_4/He was introduced into the capillary microreactor, where the catalyst was exposed to isothermal methane splitting conditions at 873 K, with the outlet composition continuously monitored by mass spectrometry. Fig. 6**c** shows the time-resolved evolution of the XRD patterns. Swiftly after introducing CH_4 into the cell, a narrowing of the diffraction signals for Ni^0 was apparent, indicating crystallite growth. No other nickel phases could be detected, ruling out the development of nickel carbide phases under the applied reaction conditions. This profile narrowing coincided with the detection of H_2 production at the reactor's outlet and the emergence of a diffraction peak at 15.8° (2θ), assigned to the (002) crystalline plane in graphite, signifying the formation of CNT/CNF. The growth of Ni nanocrystals becomes clearly evident when comparing the diffraction profile for Ni(111) right before and after exposure to methane splitting conditions (Fig. 6**e**). Profile fitting analyses[40] revealed a shift in the crystallite size distribution towards larger sizes (Fig. 6**e**), in correspondence with the *ex situ* TEM inspection discussed earlier. Remarkably, the growth of metal crystallites was absent when the as-activated catalyst underwent treatment under an inert He atmosphere at the reaction temperature of 873 K (Fig. 6**d** and **e**). These findings provide compelling evidence that it is the initial stages of the methane splitting reaction that trigger metal sintering.

Metal crystallite growth may occur according to two primary mechanisms[41,42], i.e., particle migration and coalescence or *Ostwald ripening*[43]. The latter mechanism involves the emission and collection of individual metal atoms from and onto static metal nanoparticles and is typically mediated by mobile, molecular metal complexes that migrate in the vapor phase or on the catalyst surface[44]. Size-dependent differences in surface energy enforce a net transport from smaller crystals, which shrink in size and may eventually vanish, to larger crystals, which grow at expense of the former. The observation that the growth of nickel nanocrystals is chemically stimulated under methane splitting conditions, whilst it does not proceed under reducing (H_2/He) or inert (He) gas atmospheres, suggests that the process occurs via Ostwald ripening.

Further insights into the catalysis-driven nanocrystal growth have been gained through periodic Density Functional Theory (DFT) calculations. Under the oxygen-free reaction conditions relevant to the CMS process, the formation of volatile metal polycarbonyl compounds, e.g. $Ni(CO)_4$, is ruled out. Therefore, the detachment of metal atoms from the surface of the nanocrystal, emission and migration on the surface of the Al_2O_3 carrier material have been considered, as schematically depicted in Fig. 7. Different (hydro)carbonaceous (C_xH_y) species, which may form on the catalyst surface via methane splitting and subsequent C-C coupling, have been evaluated for their potential to facilitate (assist) the elementary steps of Ni atom detachment and emission onto the Al_2O_3 carrier.

In the first step, Ni atoms detach from the surface of the metal crystallites, forming a metal adatom and leaving a lattice vacancy behind. As illustrated in Fig. 8**a**, several initial states have been considered, encompassing a perfect Ni(111) surface, which models extended metal terraces, as well as surface Ni step-edges and kinks, which emulate surface defects wherein Ni atoms are coordinatively more unsaturated. Moreover, several C_xH_y species have been screened for their potential role in both metal atom *shuttling* and vacancy *healing* elementary steps (Figure S13). These include C_1 fragments derived from CH_4 dehydrogenation, i.e. CH_3, CH_2, CH, C, as well as C_2 species, such as C_2H (acetylide) and C_2H_2 (acetylene), which may form via C-C coupling from the former. Additionally, for those species leading to the most favorable Ni atom detachment, conditions mimicking low and high ligand coverages have been considered (see Supplementary computation methods in the Supporting Information).

Fig. 8**d,e** depict the formation energy of Ni adatoms adsorbed on a Ni (111) terrace, detached from either a perfect Ni(111) facet or from a surface kink defect. Results for the intermediate situation of a Ni atom originating from a surface step-edge, as well as considering low ligand surface coverage are provided in Figures S14 and S15, respectively, in the Supporting Information. The results are presented for both unassisted atom detachment and cases where the process is mediated by various molecular species through atom *shuttling*, vacancy *healing*, or combined *shuttling* and *healing* mechanisms. Irrespective of the assisting mechanism and the degree of surface coverage of the (hydro)carbonaceous species, the detachment of a Ni atom was consistently found to be energetically most favorable from a surface kink, as it involves the disruption of fewer Ni-Ni bonds. C_xH_y species may act as ligands to Ni atoms, reducing the energy penalty associated to the undercoordination of the detached Ni atoms and those around the ensuing lattice vacancies. As observed in Fig. 8**e**, carbon adatoms (*C) significantly facilitate Ni atom detachment via a combined *shuttling* & *healing* process, while the remaining C_xH_y species resulted in endothermic atom detachment, with energy penalties (ΔE_d) notably greater than the background thermal energy under CMS conditions (ca. 0.08 eV). Particularly when more than one *C collectively bind to a single Ni atom, at the high carbon surface coverage which is expected under methane splitting conditions, the detachment of Ni atoms from low coordination positions was found to be energetically favorable, with ΔE_d of −0.52 and −1.03 eV from

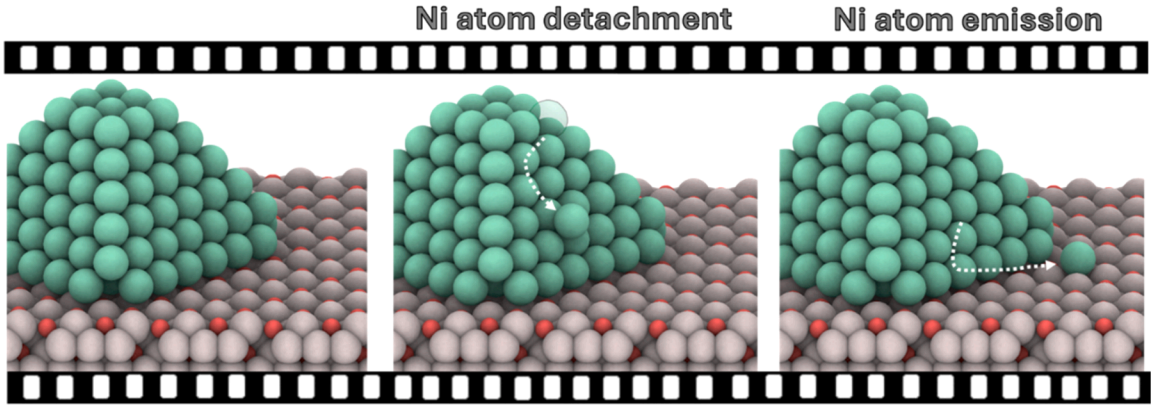

Fig. 7. Schematic representation of elementary processes of Ni atom detachment and emission from a supported Ni nanocrystal onto the surface of the Al_2O_3 support material, considered herein for an Ostwald ripening metal particle growth mechanism mediated by surface diffusion. For simplicity, the process is illustrated in its unassisted fashion, i.e., no ligands considered.

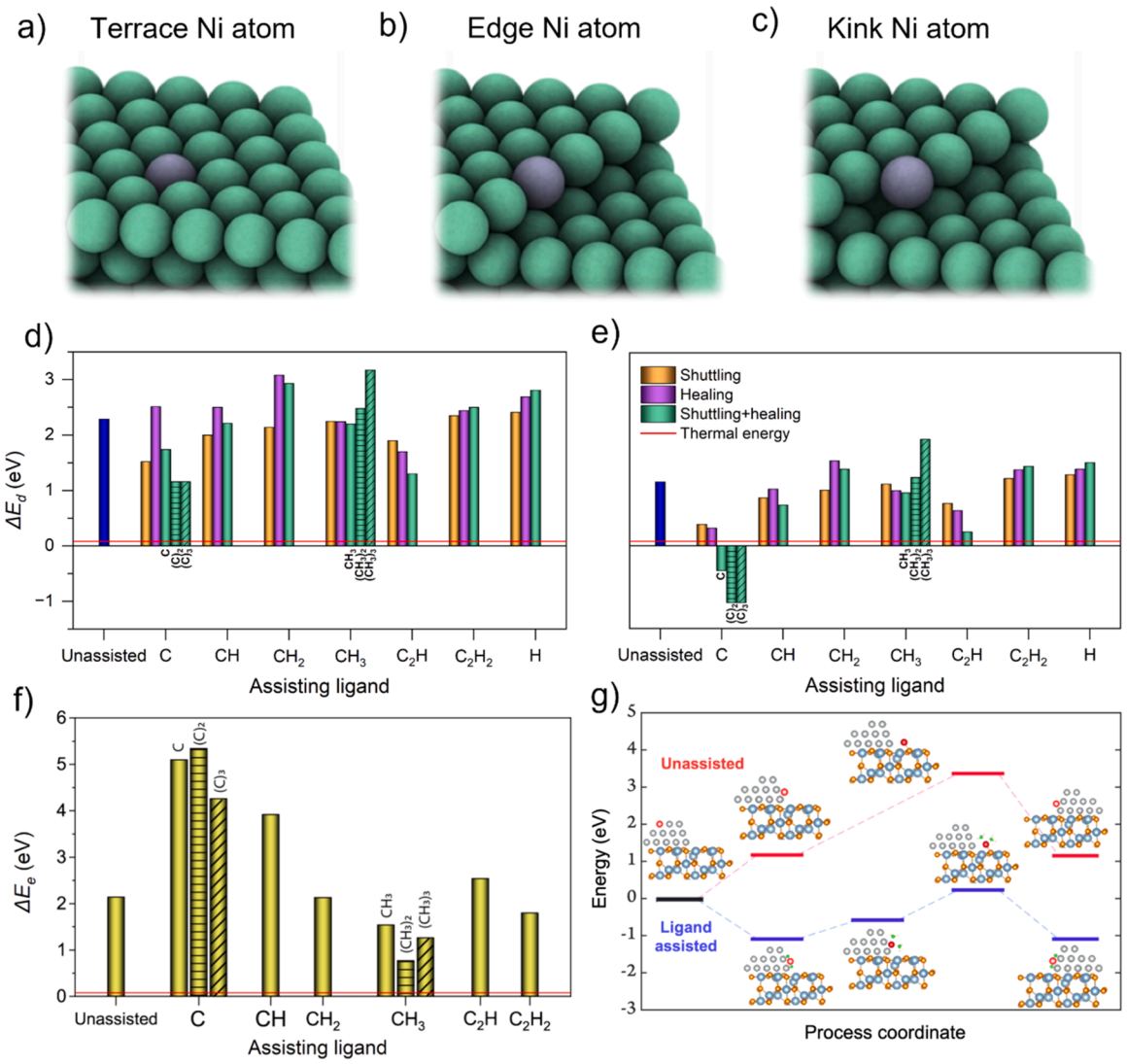

Fig. 8. a-c) Schematic representation of different types of Ni atoms considered to assess the energetics of atom detachment, i.e., **a)** atom within a perfect Ni(111) surface, **b)** atom at a surface step-edge and **c)** atom at a surface kink. **d,e)** Atom detachment energy change (ΔE_d) from **d)** a perfect Ni(111) facet and **e)** a surface kink defect as a function of the C_xH_y assisting species considered, at high surface coverages, and the assistance mechanism, i.e., atom *shuttling*, vacancy *healing* or combined *shuttling* & *healing*, as predicted by DFT calculations (PAW-PBE). **f)** Atom emission energy change (ΔE_e) for a single Ni atom from atop a Ni(111) surface onto a γ-Al_2O_3(100) surface as a function of the C_xH_y *shuttle* species considered, as predicted by DFT calculations (PAW-PBE). See Fig. S17 in the Supporting Information for details on the optimized structures considered on the γ-Al_2O_3(100) surface. In panels **d-f)**, the energetics computed for the unassisted atom emission process are also shown as reference. **g)** Total DFT energy diagram summarizing the relative stabilities of the most favorable structures for atom detachment, emission and attachment steps along an Ostwald ripening process (surface migration on the alumina surface has not been modelled). The figure shows overall energy changes, hence the E-diagram should not be interpreted as a mechanism, as energy barriers involved in the transition between these structures are not accessible. In panels d-f the horizontal red line marks the background thermal energy under methane splitting process conditions ($T = 873$ K).

metal surface step-edges and kinks, respectively. These results align with earlier findings, which suggested that coordinatively unsaturated Ni atoms at surface step-edges favor the complete dehydrogenation of CH_4, owing to the substantial stability provided to the *C product through a five-coordinated bonding with metal atoms at the step-edge. Therefore, carbon adatoms are proposed to play a central role in the detachment of metal atoms from surface defects on the Ni nanocrystals under CMS conditions.

Next, the emission of Ni atoms from the surface of the metal nanocrystals onto the alumina support was investigated. A single Ni adatom adsorbed on a Ni(111) terrace was considered as the starting configuration, whereas the oxide carrier was modeled by a γ-Al_2O_3(100) slab (Figure S16)[45]. Given that methane splitting proceeds under dry conditions at 873 K, a dehydroxylated surface has been considered to best emulate the surface of the alumina support under process conditions. Also in this case, various C_xH_y species have been studied as potential *shuttles* for atom emission, while multi-ligand coordination has been considered for *C and *CH_3, given that these fragments were found to be most favorable for metal atom detachment (*vide supra*) and emission (*vide infra*), respectively. Out of all the screened complexes, the formation of $Ni(CH_3)_2$ resulted in the lowest energy cost for Ni atom emission, with ΔE_e of 0.77 eV, ca. 1/3 of that predicted for the unassisted process (Fig. 8**f**). In contrast, the binding of *C adatoms significantly impedes the process, leading to $\Delta E_e \geq 5$ eV, i.e., more than twofold higher than that for the unassisted emission process of a naked Ni adatom.

The more favorable energetics for the emission of $Ni(CH_3)_2$ complex compared to $Ni(C)_2$ can be attributed to the structure of the latter species on the metal terrace, wherein carbon atoms are bonded both to the detached Ni adatom as well as to Ni atoms at the underlying terrace. As a

result, emission onto the γ-Al_2O_3 surface requires breaking multiple C-Ni bonds, which is not compensated by forming any suitable bond with the oxide support. Conversely, in the case of the $Ni(CH_3)_2$ complex, carbon is saturated and does not bind strongly with Ni atoms at the metal terrace. Therefore, the energy cost of emitting this complex is primarily due to the better coordination of the migrating Ni atom to other Ni atoms at the metallic terrace compared to the γ-Al_2O_3 surface. In all cases considered, the Ni atom emission process entails an energy penalty (ΔE_e>0). Therefore, the reverse process, i.e., the transfer of said mononuclear metal complex from the Al_2O_3 support onto the surface of a receiving metal nanocrystal, as required for the net particle growth mechanism, is predicted to be exothermic.

The fact that different ligands have been identified as preferred for Ni atom detachment (*C) and emission (*CH_3) elementary processes would require an additional ligand exchange process. Therefore, ligand exchange, i.e., the conversion of $Ni(C)_2$ to $Ni(CH_3)_2$, has also been studied on the terrace-adsorbed mononuclear Ni complexes. This process was found to face an energetic cost of 1.59 eV, which is significantly smaller than the > 5 eV emission energy difference predicted for $Ni(C)_2$.

Additionally, the carbon atoms released in the *C-*CH_3 swap can either contribute to growing graphitic carbon structures on the Ni surface or migrate inside the Ni nanoparticle, e.g., occupying an interstitial site. Both processes are accompanied by an energy gain of ~ 0.55 eV per carbon atom, lowering the overall energetic cost of the emission step to ~ 0.49 eV.

Fig. 8**g** summarizes the energetics predicted for the most favorable structures involved in the overall process of Ni atom detachment and emission. The notable difference between the energy profiles for the unassisted and ligand-assisted processes clearly underscores how C_1 (hydro)carbonaceous fragments from CH_4 splitting can significantly reduce the overall energy penalty for the ejection of individual Ni atoms from the Ni nanocrystals onto the Al_2O_3 support. These findings provide a rational explanation for the catalysis-driven Ni particle growth observed experimentally during the initial stages of the methane splitting reaction, which is crucial for determining the Ni particle size distribution on the working catalyst and, consequently, the overall methane splitting rate.

4. Conclusion

Catalytic methane splitting on the surface of Ni nanocrystals shows an unconventional particle size dependence, wherein an optimal Ni nanocrystal size of ca. 10 nm leads to a maximum specific hydrogen production rate. Using a set of model supported Ni catalysts with varying initial Ni nanoparticle sizes, *operando* X-ray diffraction (XRD) and post-catalysis activity-specific transmission electron microscopy studies linked the observed metal particle size effects on activity to the differing roles of Ni nanocrystals with sizes above and below 10 nm. This nanoparticle diameter marks a critical threshold for the nucleation and growth of graphitic carbon filaments, lifting the Ni nanoparticles from the surface of the oxide carrier material, which is essential for a sustained hydrogen production. In contrast, premature carbon encapsulation of smaller Ni nanoparticles, which remain static on the catalyst surface, prevents their contribution to the overall hydrogen production rate. Additionally, *operando* XRD reveals that metal nanocrystal growth is not thermally driven but initiated by early methane splitting events on the catalyst surface, which influence the extent of metal aggregation, therefore the abundance of Ni nanoparticles with sizes above and below the 10 nm threshold value and the methane splitting activity of the working catalyst. Density Functional Theory studies have identified *C and *CH_3 species, formed as part of methane dissociation on neat Ni surfaces, as key *ligands* in creating energetically more favorable conditions for Ni adatom detachment from coordinatively unsaturated sites on metal nanocrystals and their emission onto the oxide (Al_2O_3) support materials, effectively driving an Ostwald ripening mechanism. The results provide new insights into the complex carbon-metal dynamics which is at play during methane splitting, of significance for CO_x-free hydrogen production as energy vector and industrial reducing agent, with concomitant carbon *fixation* in the form added-value graphitic nanostructures. More broadly, these findings may contribute towards a rational catalyst design for other gas-to-solid conversion processes catalyzed by finely dispersed metals.

CRediT authorship contribution statement

Niloufar Atashi: Writing – original draft, Methodology, Investigation, Formal analysis, Data curation, Conceptualization. **Adrià Palomares:** Writing – original draft, Methodology, Investigation, Formal analysis, Conceptualization. **Nicola Verziaggi:** Writing – original draft, Methodology, Investigation, Formal analysis, Data curation, Conceptualization. **Luis Alves:** Methodology, Investigation, Formal analysis, Conceptualization. **Adelio Mendes:** Writing – review & editing, Supervision, Project administration, Investigation, Conceptualization. **Simone Meloni:** Writing – original draft, Supervision, Methodology, Investigation, Formal analysis, Data curation, Conceptualization. **Gonzalo Prieto:** Writing – review & editing, Supervision, Project administration, Methodology, Funding acquisition, Formal analysis, Conceptualization.

Declaration of Competing Interest

The authors declare that they have no known competing financial interests or personal relationships that could have appeared to influence the work reported in this paper.

Acknowledgements

This work has received funding from the European Commission under the Horizon 2020 programme FETPROACT-EIC-05–2019 (grant agreement Nr. 952219, 112CO2). Specific contributions have additionally received funding from the European Research Council, ERC-CoG grant, grant agreement Nr. 864195, and the Advanced Materials programme supported by the MCIN with funding from the European Union NextGenerationEU (PRTR-C17.I1) and by Generalitat Valenciana (MFA/2022/012). Financial support by the Spanish Ministry of Science and Innovation grant numbers PID2022–140111OB-I00 and CEX2021–001230-S funded by MCIN/AEI/10.13039/501100011033 is also acknowledged. Benchtop synchrotron radiation research instrumentation applied in this study has been developed within the CSIC Interdisciplinary Thematic Platform (PTI+) Transición Energética Sostenible+ (PTI-TRANSENER+) as part of the CSIC program for the Spanish Recovery, Transformation and Resilience Plan funded by the Recovery and Resilience Facility of the European Union, established by the Regulation (EU) 2020/2094. A. Palomares acknowledges CSIC for a JAE-Intro fellowship (Nr. JAEINT-22-EX-0795) for undergraduates. Authors are beholden to Sasol Materials for the provision of high-purity Al_2O_3 precursors. The *operando*, high-resolution XRD experiment has been performed at the NOTOS beamline of the ALBA Synchrotron Light Source, Spain with assistance from ALBA staff. C. Escudero, E. Villalobos, G. Agostini and C. Marini are greatly acknowledged for assistance with cell validation and experiment setup. M. Tadeo and A. Ferrero, A. Muñoz and M. Arribas (ITQ) are acknowledged for contributions to N_2 physisorption, Raman spectroscopy and H_2 chemisorption experiments, respectively. J. Prieto is acknowledged for contribution to artwork design. N.V. acknowledges the CINECA award under the ISCRA initiative, for availability of high-performance computing resources and support. Staff members of the Electron Microscopy department at the UPV are acknowledged for training, support and maintenance of electron microscopy facilities.

Appendix A. Supporting information

Supplementary data associated with this article can be found in the online version at doi:10.1016/j.apcatb.2025.125817.

Data availability

Data will be made available on request.

References

[1] A.M. Amin, E. Croiset, W. Epling, Review of methane catalytic cracking for hydrogen production, Int J. Hydrog. Energy 36 (2011) 2904–2935, https://doi.org/10.1016/j.ijhydene.2010.11.035.

[2] L. Alves, V. Pereira, T. Lagarteira, A. Mendes, Catalytic methane decomposition to boost the energy transition: scientific and technological advancements, Renew. Sustain. Energy Rev. 137 (2021) 110465, https://doi.org/10.1016/j.rser.2020.110465.

[3] J. Diab, L. Fulcheri, V. Hessel, V. Rohani, M. Frenklach, Why turquoise hydrogen will be a game changer for the energy transition, Int J. Hydrog. Energy 47 (2022) 25831–25848, https://doi.org/10.1016/j.ijhydene.2022.05.299.

[4] A. Swartbooi, K.K. Kapanji-Kakoma, N.M. Musyoka, From biogas to hydrogen: a Techno-Economic study on the production of turquoise hydrogen and solid carbons, Sustain. (Switz.) 14 (2022), https://doi.org/10.3390/su141711050.

[5] N. Sánchez-Bastardo, R. Schlögl, H. Ruland, Methane pyrolysis for Zero-Emission hydrogen production: a potential bridge technology from fossil fuels to a renewable and sustainable hydrogen economy, Ind. Eng. Chem. Res 60 (2021) 11855–11881, https://doi.org/10.1021/acs.iecr.1c01679.

[6] G. Chen, X. Tu, G. Homm, A. Weidenkaff, Plasma pyrolysis for a sustainable hydrogen economy, Nat. Rev. Mater. 7 (2022) 333–334, https://doi.org/10.1038/s41578-022-00439-8.

[7] L. Fulcheri, V.-J. Rohani, E. Wyse, N. Hardman, E. Dames, An energy-efficient plasma methane pyrolysis process for high yields of carbon black and hydrogen, Int J. Hydrog. Energy 48 (2023) 2920–2928, https://doi.org/10.1016/j.ijhydene.2022.10.144.

[8] J. Prabowo, L. Lai, B. Chivers, D. Burke, A.H. Dinh, L. Ye, Y. Wang, Y. Wang, L. Wei, Y. Chen, Solid carbon co-products from hydrogen production by methane pyrolysis: current understandings and recent progress, Carbon N. Y 216 (2024) 118507, https://doi.org/10.1016/j.carbon.2023.118507.

[9] L. Alves, V. Pereira, S. Delgado, N. Atashi, P. Dias, T. Lagarteira, G. Prieto, A. Mendes, Regeneration of methane splitting catalysts by interfacial hydrogenation, Chem. Eng. J. 500 (2024) 157046, https://doi.org/10.1016/j.cej.2024.157046.

[10] J.Bin Choi, J.S. Im, S.C. Kang, Y.S. Lee, C.W. Lee, Effect of metal–support interaction in Ni/SiO2 catalysts on the growth of carbon nanotubes by methane decomposition, Carbon Lett. 33 (2023) 477–488, https://doi.org/10.1007/s42823-022-00438-3.

[11] W. Ahmed, M.R. Noor El-Din, A.A. Aboul-Enein, A.E. Awadallah, Effect of textural properties of alumina support on the catalytic performance of Ni/Al2O3 catalysts for hydrogen production via methane decomposition, J. Nat. Gas. Sci. Eng. 25 (2015) 359–366, https://doi.org/10.1016/j.jngse.2015.05.015.

[12] A. Kaporov, O. Shtyka, R. Ciesielski, A. Kedziora, W. Maniukiewicz, M. Szynkowska-Jozwik, Y. Madeniyet, T. Maniecki, Effect of CaO, Al2O3, and MgO supports of ni catalysts on the formation of graphite-like carbon species during the boudouard reaction and methane cracking, Materials 16 (2023), https://doi.org/10.3390/ma16083180.

[13] S. Takenaka, H. Ogihara, I. Yamanaka, K. Otsuka, Decomposition of methane over supported-Ni catalysts: effects of the supports on the catalytic lifetime, Appl. Catal. A Gen. 217 (2001) 101–110, https://doi.org/10.1016/S0926-860X(01)00593-2.

[14] M. Xu, J.A. Lopez-Ruiz, L. Kovarik, M.E. Bowden, S.D. Davidson, R.S. Weber, I. W. Wang, J. Hu, R.A. Dagle, Structure sensitivity and its effect on methane turnover and carbon co-product selectivity in thermocatalytic decomposition of methane over supported ni catalysts, Appl. Catal. A Gen. 611 (2021) 117967, https://doi.org/10.1016/j.apcata.2020.117967.

[15] D. Chen, K.O. Christensen, E. Ochoa-Fernández, Z. Yu, B. Tøtdal, N. Latorre, A. Monzón, A. Holmen, Synthesis of carbon nanofibers: effects of ni crystal size during methane decomposition, J. Catal. 229 (2005) 82–96, https://doi.org/10.1016/j.jcat.2004.10.017.

[16] W. Liang, H. Yan, C. Chen, D. Lin, K. Tan, X. Feng, Y. Liu, X. Chen, C. Yang, H. Shan, Revealing the effect of nickel particle size decomposition reaction, Catalysts 10 (2020) 890.

[17] S. Theme, Catal. Decompos. methane Support. Ni (2009) 814–820, https://doi.org/10.1002/apj.

[18] M. Xu, J.A. Lopez-Ruiz, L. Kovarik, M.E. Bowden, S.D. Davidson, R.S. Weber, I. W. Wang, J. Hu, R.A. Dagle, Structure sensitivity and its effect on methane turnover and carbon co-product selectivity in thermocatalytic decomposition of methane over supported ni catalysts, Appl. Catal. A Gen. 611 (2021) 117967, https://doi.org/10.1016/j.apcata.2020.117967.

[19] E. Hondo, T.Z.H. Gani, M. Kosari, S. Xi, N. Bella, J. Ashok, J.Y. Tan, T. Wang, H. Bian, K.H. Lim, L. Chen, J. Chang, A. Borgna, S. Kawi, Unveiling the roles of precursor structure and controlled sintering on Ni-phyllosilicate-derived catalysts for low-temperature methane decomposition, ACS Sustain Chem. Eng. 11 (2023) 8786–8799, https://doi.org/10.1021/acssuschemeng.3c00120.

[20] D. Chen, K.O. Christensen, E. Ochoa-Fernández, Z. Yu, B. Tøtdal, N. Latorre, A. Monzón, A. Holmen, Synthesis of carbon nanofibers: effects of ni crystal size during methane decomposition, J. Catal. 229 (2005) 82–96, https://doi.org/10.1016/j.jcat.2004.10.017.

[21] S. Helveg, C. López-Cartes, J. Sehested, P.L. Hansen, B.S. Clausen, J.R. Rostrup-Nielsen, F. Abild-Pedersen, J.K. Nørskov, Atomic-scale imaging of carbon nanofibre growth, Nature 427 (2004) 426–429, https://doi.org/10.1038/nature02278.

[22] R.T.K. Baker, P.S. Harris, J. Henderson, R.B. Thomas, Formation of carbonaceous deposits from the reaction of methane over nickel, Carbon N. Y 13 (1975) 17–22, https://doi.org/10.1016/0008-6223(75)90252-3.

[23] G.A. Somorjal, J. Carrazza, Structure sensitivity of catalytic reactions, Ind. Eng. Chem. Fundam. 25 (1986) 63–69, https://doi.org/10.1021/i100021a009.

[24] R.A. Van Santen, Complementary structure sensitive and insensitive catalytic relationships, Acc. Chem. Res 42 (2009) 57–66, https://doi.org/10.1021/ar800022m.

[25] P. van Helden, I.M. Ciobîcă, R.L.J. Coetzer, The size-dependent site composition of FCC cobalt nanocrystals, Catal. Today 261 (2016) 48–59, https://doi.org/10.1016/j.cattod.2015.07.052.

[26] J.P. Den Breejen, P.B. Radstake, G.L. Bezemer, J.H. Bitter, V. Frøseth, A. Holmen, K.P. De Jong, On the origin of the cobalt particle size effects in Fischer-Tropsch catalysis, J. Am. Chem. Soc. 131 (2009) 7197–7203, https://doi.org/10.1021/ja901006x.

[27] E.B. Sterk, A.E. Nieuwelink, M. Monai, J.N. Louwen, E.T.C. Vogt, I.A.W. Filot, B. M. Weckhuysen, Structure sensitivity of CO2Conversion over nickel metal nanoparticles explained by micro-kinetics simulations, JACS Au 2 (2022) 2714–2730, https://doi.org/10.1021/jacsau.2c00430.

[28] J.R.A. Sietsma, H. Friedrich, A. Broersma, M. Versluijs-Helder, A. Jos van Dillen, P. E. de Jongh, K.P. de Jong, How nitric oxide affects the decomposition of supported nickel nitrate to arrive at highly dispersed catalysts, J. Catal. 260 (2008) 227–235, https://doi.org/10.1016/j.jcat.2008.10.007.

[29] D. Baizar, H. Ledbetter, Accurate modeling of size and strain broadening in the rietveld refinement: the “Double-Voigt” approach, Adv. XRay Anal. 38 (1994) 397–404, https://doi.org/DOI: 10.1154/S0376030800018048.

[30] G. Kresse, J. Furthmüller, Efficiency of ab-initio total energy calculations for metals and semiconductors using a plane-wave basis set, Comput. Mater. Sci. 6 (1996) 15–50, https://doi.org/10.1016/0927-0256(96)00008-0.

[31] G. Kresse, J. Furthmüller, Efficient iterative schemes for ab initio total-energy calculations using a plane-wave basis set, Phys. Rev. B 54 (1996) 11169–11186, https://doi.org/10.1103/PhysRevB.54.11169.

[32] G. Kresse, J. Hafner, Norm-conserving and ultrasoft pseudopotentials for first-row and transition elements, J. Phys. Condens. Matter 6 (1994) 8245–8257, https://doi.org/10.1088/0953-8984/6/40/015.

[33] D. Joubert, From ultrasoft pseudopotentials to the projector augmented-wave method, Phys. Rev. B Condens Matter Mater. Phys. 59 (1999) 1758–1775, https://doi.org/10.1103/PhysRevB.59.1758.

[34] L. Xu, K.G. Papanikolaou, B.A.J. Lechner, L. Je, G.A. Somorjai, M. Salmeron, M. Mavrikakis, Formation of active sites on transition metals through reaction-driven migration of surface atoms, Science 380 (1979) (2023) 70–76, https://doi.org/10.1126/science.add0089.

[35] R.S. Weber, M. Xu, J.A. Lopez-Ruiz, C. Jiang, J. Hu, R.A. Dagle, Toward rational design of nickel catalysts for thermocatalytic decomposition of methane for carbon dioxide-free hydrogen and value-added carbon co-product: a review, ChemCatChem 16 (2024) e202301629, https://doi.org/10.1002/cctc.202301629.

[36] R.A. van Santen, Insensitive catalytic relationships, Acc. Chem. Res 42 (2009) 57–66.

[37] T.V. Reshetenko, L.B. Avdeeva, Z.R. Ismagilov, V.V. Pushkarev, S.V. Cherepanova, A.L. Chuvilin, V.A. Likholobov, Catalytic filamentous carbon: structural and textural properties, Carbon N. Y 41 (2003) 1605–1615, https://doi.org/10.1016/S0008-6223(03)00115-5.

[38] F. Ding, K. Bolton, A. Rosén, Nucleation and growth of Single-Walled carbon nanotubes: a molecular dynamics study, J. Phys. Chem. B 108 (2004) 17369–17377, https://doi.org/10.1021/jp046645t.

[39] L.P. Ding, B. McLean, Z. Xu, X. Kong, D. Hedman, L. Qiu, A.J. Page, F. Ding, Why carbon nanotubes grow, J. Am. Chem. Soc. 144 (2022) 5606–5613, https://doi.org/10.1021/jacs.2c00879.

[40] J.I. Langford, D. Louër, P. Scardi, Effect of a crystallite size distribution on X-ray diffraction line profiles and whole-powder-pattern fitting, J. Appl. Crystallogr 33 (2000) 964–974, https://doi.org/10.1107/S002188980000460X.

[41] E. Ruckenstein, Sintering and redispersion of supported metal catalysts, in: S.S. J.B. T.-S. in, C. Bourdon (Eds.), Growth and Properties of Metal Clusters, Elsevier, 1980, pp. 57–63, https://doi.org/10.1016/S0167-2991(08)65162-9.

[42] T.W. Hansen, A.T. DeLaRiva, S.R. Challa, A.K. Datye, Sintering of catalytic nanoparticles: particle migration or ostwald ripening? Acc. Chem. Res 46 (2013) 1720–1730, https://doi.org/10.1021/ar3002427.

[43] W. Ostwald, Elektrochemie: ihre geschichte und lehre, Lehrb. der Allg. Chem. 2 (1896).

[44] R. Ouyang, J.X. Liu, W.X. Li, Atomistic theory of ostwald ripening and disintegration of supported metal particles under reaction conditions, J. Am. Chem. Soc. 135 (2013) 1760–1771, https://doi.org/10.1021/ja3087054.

[45] T.H. Chen, D.G. Vlachos, S. Caratzoulas, Ab initio molecular dynamics study of pd nucleation on a γ-Al2O3 surface, J. Phys. Chem. C. 127 (2023) 13911–13917, https://doi.org/10.1021/acs.jpcc.3c02682.